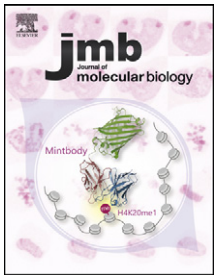

Pathogenic Mutations within the Disordered Palindromic Region of the Prion Protein Induce Structure Therein and Accelerate the Formation of Misfolded Oligomers

A.T. Sabareesan and Jayant B. Udgaonkar

National Centre for Biological Sciences, *Tata Institute of Fundamental Research, Bengaluru 560065, India*

Correspondence to Jayant B. Udgaonkar: *jayant@ncbs.res.in*
http://dx.doi.org/10.1016/j.jmb.2016.08.015
Edited by Ronald Wetzel

Abstract

Little is understood about how the intrinsically disordered N-terminal region (NTR) of the prion protein modulates its misfolding and aggregation, which lead to prion disease. In this study, two pathogenic mutations, G113V and A116V, in the palindromic region of the NTR are shown to have no effect on the structure, stability, or dynamics of native mouse prion protein (moPrP) but nevertheless accelerate misfolding and oligomerization. For wild-type moPrP, misfolding and oligomerization appear to occur concurrently, while for both mutant variants, oligomerization is shown to precede misfolding. Kinetic hydrogen–deuterium exchange–mass spectrometry experiments show that sequence segment 89–132 from the NTR becomes structured, albeit weakly, during the oligomerization of both mutant variants. Importantly, this structure formation occurs prior to structural conversion in the C-terminal domain and appears to be the reason that the formation of misfolded oligomers is accelerated by the pathogenic mutations.

Introduction

The prion protein is a Glycosylphosphatidylinositol-anchored protein, present primarily in the mammalian brain, which is responsible for the transmission and pathogenesis of a group of neurodegenerative disorders known as transmissible spongiform encephalopathies [1,2]. Conformational conversion of the native, monomeric cellular prion protein (PrP^C) into an aggregated form (PrP^{Sc}) is associated with disease pathology and neurodegeneration [3]. PrP^C has an unstructured N-terminal region (NTR; residues 23–120) and a structured C-terminal domain (CTD; residues 121–231) [4]. The structure of PrP^{Sc} remains poorly defined, but it has been shown that residues 90–230 form the protease-resistant core of PrP^{Sc} [2,5].

Despite the well-known role of the conformational conversion of PrP^C in prion pathogenesis, the mechanism of this conversion and the final structure of the misfolded PrP are poorly understood. Generally, prion diseases occur spontaneously or are transmitted from individuals infected with prion disease. Nevertheless, familial forms of prion diseases can occur, due to specific mutations in the *PRNP* gene that codes for the prion protein. These disease-causing mutations are localized mainly in helix 2 (α2) and helix 3 (α3) of the structured CTD and in sequence segment 105–126, known as the middle hydrophobic core region of the unstructured NTR [6]. Several pathogenic mutations found in the CTD reduce the thermodynamic stability and increase the native state dynamics of the prion protein [7–9]. However, other pathogenic mutations like E199K, V209I, and T189V (mouse numbering; mouse numbering is used throughout this article), which occur in the α3 region, do not affect the stability of PrP [8]. Hence, it appears that the destabilization of PrP^C, leading to the formation of aggregation-competent intermediates, may not be a general mechanism for the formation of PrP^{Sc} [8].

In the unstructured NTR of the prion protein, the middle hydrophobic region is the main hotspot for mutations associated with familial forms of prion diseases. This region has been shown to play an important role in the conformational conversion of the prion protein [10,11]. In particular, a palindromic sequence in this segment spanning residues 111–120 (VAGAAAAGAV) has been implicated to play a role in the assembly of fibrils and in the structural changes accompanying prion conversion [12–14]. Additionally, it appears that this segment is essential

for the productive association of PrP^C with PrP^{Sc}, which leads to prion propagation in animals [15]. In the middle hydrophobic region, the P104L, G113V, A116V, and G130V mutations have been linked to the Gerstmann–Sträussler–Scheinker (GSS) syndrome [3,6]. However, the mechanism by which these mutations lead to prion pathogenesis remains unclear [16].

It has been difficult to study how mutations that occur in the unstructured NTR affect the global structure of PrP, as well as the conformational conversion of PrP, due to the intrinsically disordered nature of the NTR [4]. Several effects of these mutations have been reported. The A116V mutation has been reported to facilitate the formation of a transmembrane form of PrP, which leads to neurodegeneration without any detectable accumulation of PrP^{Sc} [17,18]. In fact, a recent study has shown that this mutation enhances ion-selective channel formation by the mouse prion protein (moPrP) [19]. The P101L and P104L mutant variants have been reported to form fibrils with an N-terminally extended amyloid core [20]. An *in vivo* study has reported that the G113V and A116V mutations lead to the formation of a protease-sensitive PrP conformation with a high degree of neurotoxicity [21]. The mechanisms by which mutations in this region affect the conformational conversion of PrP remain, however, unclear. Clearly, it has become important to study the effects of mutations in the unstructured NTR, particularly in the palindromic sequence, to obtain a better understanding of its role in the conformational conversion of PrP.

Results and Discussion

The pathogenic mutations G113V and A116V do not affect the structure and stability of native monomeric moPrP

In the current study, the effects of two GSS syndrome-associated pathogenic mutations, which are found in the palindromic region of PrP, G113V, and A116V (Fig. 1), on the structure, stability, and misfolding of moPrP were characterized. Figures 2 and 3 show that the G113V and A116V mutations did not affect the structures and stabilities of moPrP. The circular dichroism (CD) spectra (Fig. 2a), the Fourier transform infrared (FTIR) spectra (Fig. 3), and the dynamic light scattering (DLS) profiles (Fig. S1) of wild-type (wt), G113V, and A116V moPrP were found to be very similar to each other. Denaturant-induced equilibrium unfolding studies indicated that the three moPrP variants had identical thermodynamic stabilities at pH 4 (Fig. 2b) and at pH 7 (Fig. 2d) and had identical midpoints for their thermally induced unfolding transitions at pH 4 (Fig. 2c). Hence, the G113V and A116V mutations in the unstructured NTR did not, unsurprisingly, affect the global stability of moPrP [22].

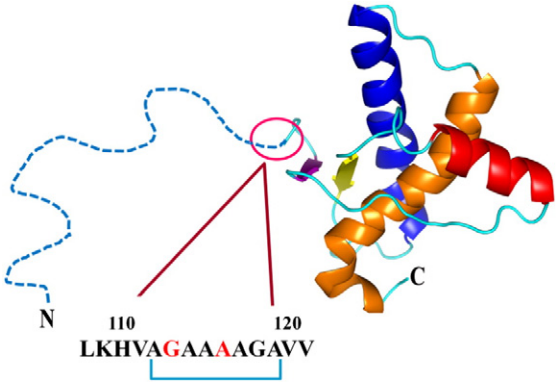

Fig. 1. Structure of the full-length (23–231) moPrP. The CTD of the prion protein was drawn using PyMOL and the PDB file 1XYX. The NTR (23–120) is known to be unstructured in the full-length protein and is drawn as a random coil. The mutation sites are marked in the sequence.

In an earlier study [23], another nearby pathogenic mutation, P101L, in the NTR had also been shown to not affect the structure and dynamics of moPrP. It became important to determine whether the G113V and A116V mutations had an effect on misfolding and aggregation, even though they did not affect global structure and stability.

The pathogenic mutations G113V and A116V accelerate the formation of misfolded oligomers

The prion protein is known to misfold and oligomerize not only on the cell surface but also in the endocytic pathway, where it encounters low pH [24]. In earlier studies [25,26], it had been shown that moPrP remains native at pH 4 but becomes prone to misfolding because the critical residue His186 has become protonated [27]. Misfolding and oligomerization can then be triggered by the addition of salt [25]. In this study, the kinetics of misfolding of wt, G113V, and A116V moPrP were monitored by the measurement of CD change, and the kinetics of oligomerization were monitored by size-exclusion chromatography (SEC) at pH 4, upon the addition of 150 mM NaCl (Fig. S2). It should be noted that the formation of misfolded oligomers at low pH correlates well with the propensity to get prion disease [28]. Such oligomers have been shown to be capable of disrupting membrane structure [25] and also to be capable of forming worm-like amyloid fibrils [25,29].

As shown previously, the kinetics of CD-monitored conformational change and SEC-monitored oligomerization of 100 μM wt MoPrP were identical at pH 4 in the presence of 150 mM NaCl (Fig. 4a). The observed rate matched to that reported earlier [25]. In contrast, in the case of both 100 μM G113V and A116V moPrP, the rate of SEC-monitored oligomerization was twofold higher than the rate of CD-monitored

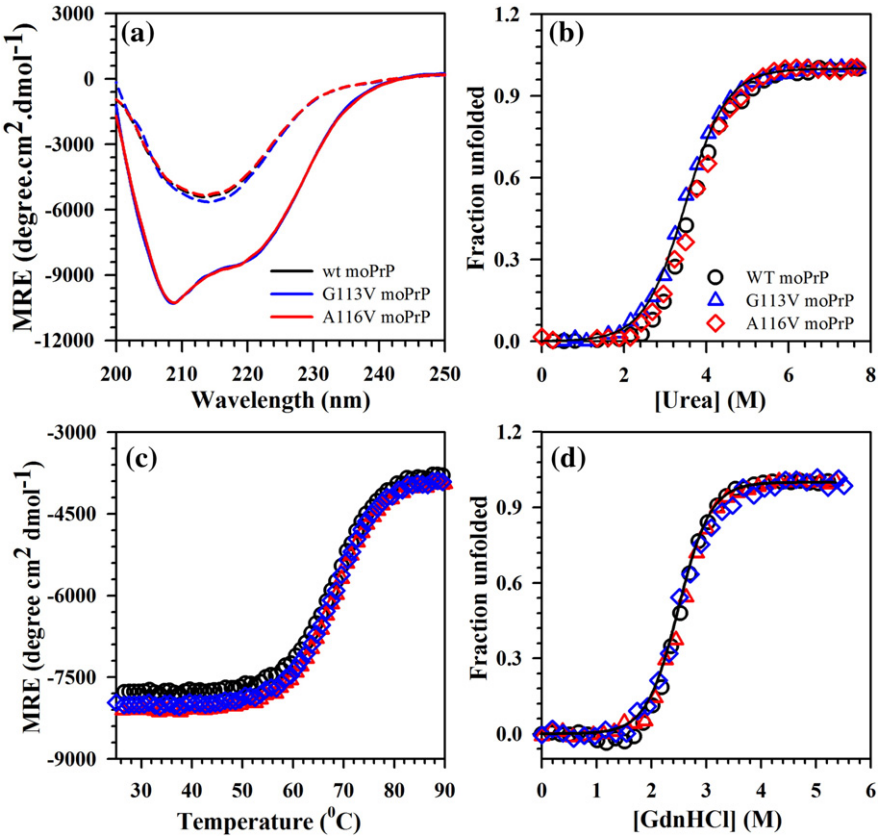

Fig. 2. Spectroscopic characterization of structures and stabilities of the moPrP variants. (a) Far-UV CD spectra of native monomeric (solid line) and misfolded oligomeric (dashed line) forms of moPrP variants monitored at pH 4. Oligomerization of moPrP variants was carried out in the presence of 150 mM NaCl at 37 °C (pH 4). (b) Thermodynamic stabilities of native monomeric wt, G113V, and A116V moPrP at pH 4. Urea-induced equilibrium unfolding transitions at pH 4 and 25 °C as monitored by Far-UV CD at 222 nm are shown. (c) Thermally induced unfolding of the moPrP variants at pH 4 as monitored by far-UV CD at 222 nm. (d) GdnHCl-induced equilibrium unfolding transitions at pH 7 and 25 °C as monitored by far-UV CD at 222 nm. The continuous lines through the data points in (c) were drawn by inspection to guide the eye. In (b and d), the signals were normalized to obtain the fraction unfolded.

misfolding and was about eightfold higher than the rate of SEC- and CD-monitored oligomerization of wt moPrP (Figs. 4a–c and S2). For each of the three moPrP variants, the rates of CD-monitored conformational change were the same, whether monitored at 208, 216, or 222 nm (Fig. S3). The faster aggregation reactions of G113V and A116V moPrP were seen over the entire range (10–100 μM) of protein concentrations studied (Fig. 4d–f). These results suggested that oligomerization preceded misfolding in the case of G113V and A116V. For these two mutant variants, it is clear that misfolding occurs predominantly in oligomerized protein. In the case of wt moPrP, misfolding and oligomerization either occurred concurrently or oligomerization was rate limiting and followed by fast misfolding (see below). Such a two-step mechanism of association followed by conformational change is similar to that proposed earlier for the huntingtin protein [30]. It should, however, be noted that for all three moPrP variants, it is likely that dimerization was itself accompanied, or indeed driven, by conformational change. If this change were relatively minor and restricted to a short sequence stretch in the unstructured NTR or in a loop of the CTD, it is unlikely that it would be picked up by the measurement of a probe of gross structural change such as CD.

The rate-limiting step in the formation of misfolded oligomers is the dimer formation

The reaction orders for the misfolding and oligomerization reactions of all three mutant variants were determined from the slopes of the plots of the logarithm of initial rates *versus* the logarithm of protein concentration (Figs. 4d–f and S4; see Materials and Methods), which were ~1 in all cases. Hence, the reaction order was determined, using Eq. (1), to be two, indicating that the rate-limiting step in misfolding and oligomerization is the formation of a dimer. In fact,

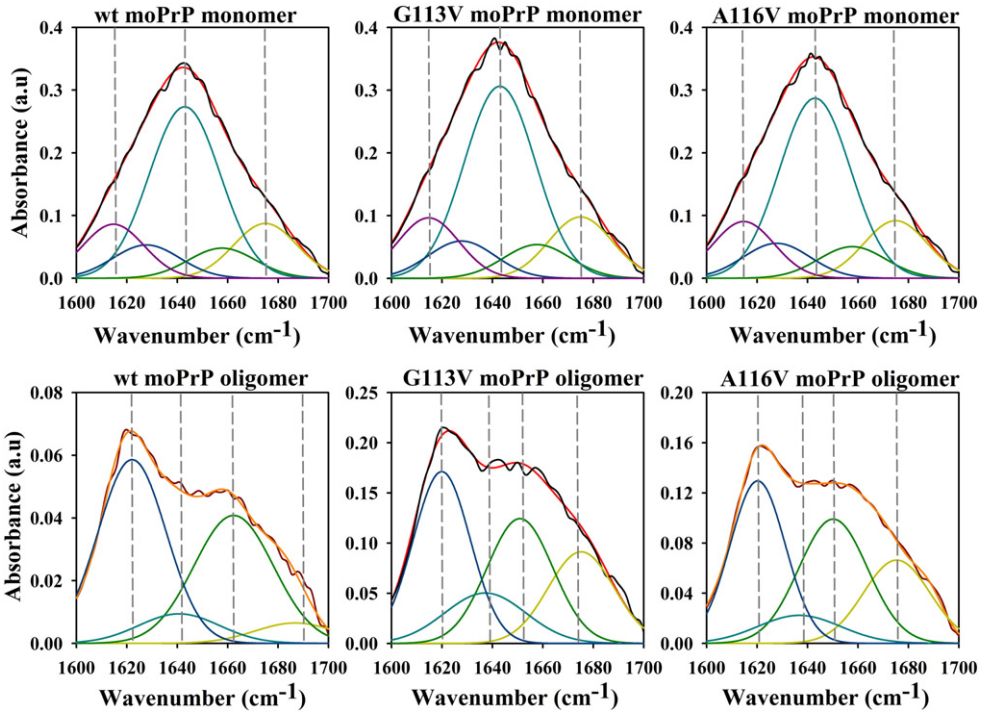

Fig. 3. Structural characterization of the moPrP variants. The amide I regions (1600–1700 cm^{-1}) of the FTIR spectra of the native moPrP variants (upper panel) and oligomeric moPrP variants (lower panel) are shown. FTIR spectra of the native proteins at pH 4 were acquired at 1 mM protein concentration, and the oligomeric proteins at pH 4 were acquired in the presence of 150 mM NaCl. Experimental spectra are displayed as black lines. The deconvoluted spectra are displayed as colored lines. Their sum is represented as a red line that overlaps the experimental data closely. The peaks at ~1620 cm^{-1}, ~1645 cm^{-1}, ~1660 cm^{-1}, and ~1675 cm^{-1}arise from amyloid cross-β, helical, disordered, and β-sheet structure, respectively [53].

the association of PrP^C *via* the palindromic region is known as a critical event that initiates PrP^{Sc} formation [15]. Mutations occurring in this region are therefore likely to affect the initial interaction between two monomeric PrP molecules.

The pathogenic mutations G113V and A116V induce weak structure in the middle hydrophobic region of oligomeric protein

To understand the structural basis of why both mutant variants misfold and oligomerize faster than wt moPrP, the native monomer as well as the misfolded oligomer formed by wt, G113V, and A116V moPrP were characterized by hydrogen–deuterium exchange (HDX) in conjunction with mass spectrometry (MS). HDX differentiates between the structured regions that are protected against exchange and the unstructured regions that are unprotected. Less deuterium gets incorporated into more stable segments, and more deuterium in less stable segments. Since a sequence segment that is labeled by deuterium has a higher mass than when it is unlabeled, labeled segments are easily identifiable by MS by carrying out peptic fragmentation after exchange [31]. Fortunately, pH 4, at which moPrP readily misfolds and oligomerizes upon the addition of salt, is close to the pH at which HDX is the slowest; this allows the structural changes in all secondary structural units of the protein to be followed [32].

The HDX–MS method enables the measurement of the local stabilities of all secondary structural units by determining the kinetics of deuterium incorporation into the sequence segments that fold to form the secondary structures. In Fig. 5, it is seen that these kinetics were identical for the native form of wt, G113V and A116V moPrP, for HDX into each sequence segment at pH 4, in the absence of added salt. Hence, the G113V and A116V mutations, like the P101L mutation studied earlier [33], had little effect on the local structural dynamics of the native protein, particularly in the structured CTD.

To understand how the G113V and A116V mutations accelerate misfolding, it was necessary to study the structures of the oligomers formed at the end of the aggregation process and to characterize structurally and kinetically the aggregation process itself. Under the conditions (pH 4 and 37 °C) in which the proteins

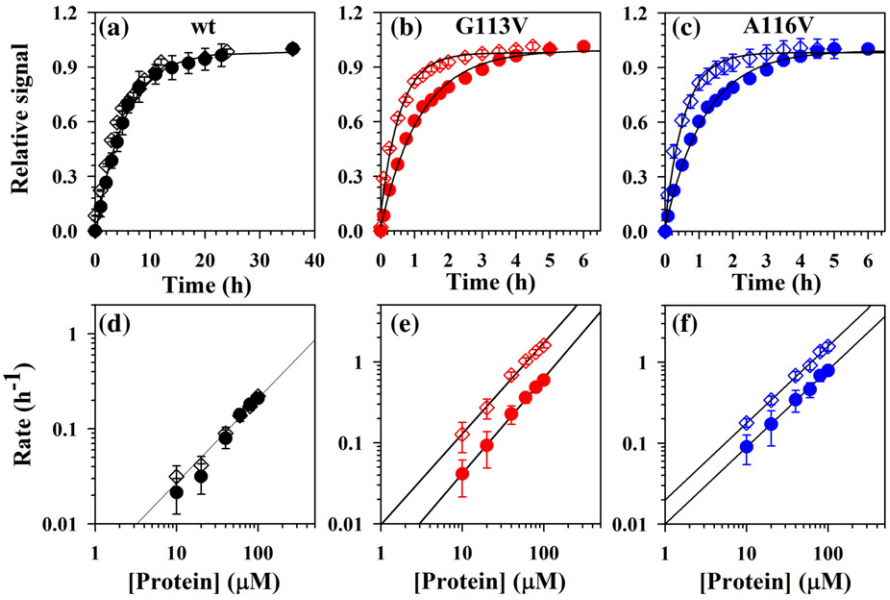

Fig. 4. Misfolding and oligomerization of the moPrP variants. The kinetics of misfolding and oligomerization were monitored using far-UV CD at 222 nm (•) and SEC (◊) for (a) wt moPrP, (b) G113V moPrP, and (c) A116V moPrP. Misfolding and oligomerization were carried out in the presence of 150 mM NaCl at 37 °C (pH 4) and at 100 μM protein concentration. Data were normalized to values between 0 (corresponding to 100% monomer) and 1 (corresponding to 100% oligomer). (d–f) Plots of the logarithm of the misfolding/oligomerization rate *versus* the logarithm of the protein concentration for wt, G113V, and A116V moPrP, respectively. The straight lines through the data in each panel are linear fits with slopes of (d) 0.9, (e) 1.2 and 1.12, and (f) 0.9 and 1.0. In each panel, the error bars represent the standard deviations determined from three independent experiments.

misfold and oligomerize upon the addition of 150 mM NaCl, the average intrinsic rate constant for HDX into moPrP is calculated to be 0.03 s^{-1}. Hence, to distinguish between protected (stable) and unprotected (unstable) structure in both monomer and oligomer, a HDX labeling pulse of 180-s duration at pH 4 was utilized, which would completely label all unprotected structure. In addition, both shorter (30 s) and longer (2 h) labeling pulse durations were used to differentiate between structures varying in stability in monomer *versus* oligomer.

Fig. 6 shows that for all three moPrP variants, the sequence segment 182–204 stretching from α2 to the beginning of α3 in native moPrP was more protected in oligomer than in monomer. Sequence stretch 205–212, which forms the middle of α3 in native moPrP, was strongly protected in both monomer and oligomer, marginally more in the latter. On the other hand, the C-terminal end of α3 (217–223) was moderately protected in the oligomers while being strongly protected in the monomers. The sequence stretch 133–167, which forms the loop preceding α1, α1 itself, the loop separating α1 and β2, and β2 itself in native moPrP, appeared weakly protected in the oligomers but moderately protected in the monomers for all three moPrP variants.

While the HDX data indicated that the pattern and extent of HDX into all three native moPrP variants were the same, significant differences were observed between the extent of HDX into wt oligomers and into the mutant oligomers: (1) sequence stretch 89–132, which was unprotected in the wt oligomer, was weakly protected in the both mutant oligomers. (2) As was reported earlier [7,34], sequence segment 109–132 showed more conformational heterogeneity in both mutant oligomers than in wt oligomer: 20% of the protein molecules in both mutant oligomers showed protection in this segment, while only 3% did so in the wt oligomers (Fig. S5 and Table S1).

The induction of weak structure in sequence segment 89–132 in both mutant oligomers, as reflected in their increased protection against HDX (Fig. 6a) compared to wt oligomer, could be because a part or this entire region is a site for intermolecular interaction within the oligomer. Indeed, this middle hydrophobic region has been shown to be involved in intermolecular association during the aggregation of PrP [11,15]. The replacement of either Gly or Ala residue by the branched Val residue in sequence segment 89–132 is likely to have increased its propensity to form β-sheet. Indeed, the FTIR spectra of both mutant oligomers (Fig. 3) showed that they possessed a higher fraction of β-sheet structure and a lower fraction of disordered structure than did the wt oligomer. This was not surprising as the palindromic region of human PrP has been shown to be capable of

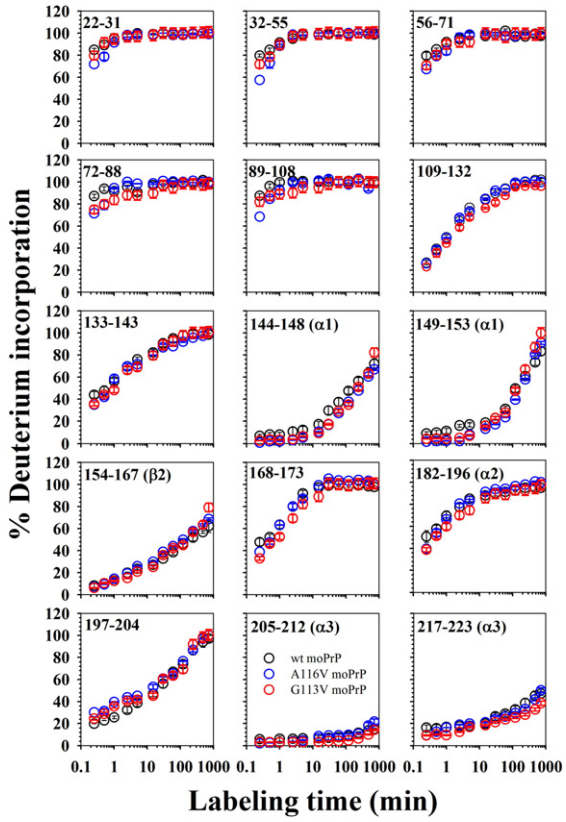

Fig. 5. Native state dynamics of moPrP variants. The kinetics of HDX into different sequence segments of native and monomeric wt, G113V, and A116V moPrP at 25 °C and pH 4 are shown. Percentage of deuterium incorporation is plotted *versus* the time for different sequence segments (see Materials and Methods). Error bars represent the standard deviations determined from three independent experiments.

adopting β-sheet structure [35]. In fact, it has been suggested that amyloid fibril formation commences from this region [36], and a peptide derived from this region readily converts into amyloid fibrils [37].

Alternatively, the induction of weakly protected structure in sequence segment 89–132 could be due to it binding to a region of the CTD, either intramolecularly or intermolecularly, within the mutant oligomers. It would then be expected that the region on the CTD to which it binds would also be more protected against HDX in mutant than in wt oligomer. The only region that is more protected, albeit weakly, against HDX in the CTD of both mutant oligomers than in the CTD of wt oligomer is sequence segment 144–153, which forms α1 in native moPrP (Figs. 7 and S6). It is, however, unlikely that sequence segment 89–132 binds to and thereby stabilizes sequence segment 144–153 in either mutant oligomer, because the stabilization of this region would have resulted in the slowing down of the misfolding and oligomerization of the mutant variants [7,38] and not in their acceleration, as was observed (Fig. 4). A third possible reason for why sequence segment 89–132 is stabilized more in both mutant oligomers could also be that the β-sheet core of the oligomer extends from residue 223 down to residue 89 in the case of a subset of both mutant oligomers. This region is known to become structured in PrP^{Sc} [10]. If the core is indeed extended, then the core of the mutant oligomers would be more similar to the core of PrP^{Sc} [39]. However, it is unlikely that the core extends continuously from residue 223 to residue 89 in the case of the mutant oligomers, because sequence stretch 133–167 was weakly protected in the oligomers for all three moPrP variants.

The HDX data suggest an explanation for why the mutant proteins misfold and oligomerize faster than the wt protein (Fig. 4), even though the global stabilities (Fig. 2) as well as the local stabilities (Fig. 5) of the three moPrP variants are the same. Both mutant oligomers are likely to be more stable than the wt oligomer because they have more structure protected against HDX, most likely because of intermolecular association at the middle hydrophobic region (see above). The free energy barrier to the aggregation of the mutant variants would be less if the additional stabilizing structure is also present in the highest energy state during oligomerization.

The observation that sequence segment 89–132 is stabilized in both mutant oligomers, compared to that in the wt oligomer (Fig. 6a), can be used to rationalize why the rate of oligomerization is faster than the rate of misfolding for both mutant moPrP variants but not for wt moPrP (Fig. 4). It appears that the induction of structure in this region in the case of the mutant moPrP variants accelerates association, resulting in it preceding conformational conversion (Fig. 8).

The data in Fig. 4 reveal the structural changes that occur in different sequence segments when monomer converts into oligomer. The FTIR data (Fig. 3) indicate a very significant loss of helical structure in the oligomers and an increase in the cross-β-sheet, characteristic of the amyloid structures [40,41]. Marginal, apparent helical structure has been claimed to be present in PrP^{Sc} too [42,43], although this claim has been contested [39]. The HDX data indicate that α1 of native monomer has unfolded in the oligomers, in agreement with earlier results [34,44], and that α2 and part of α3 have likely converted to β-sheet, as suggested by the observation that the sequence stretching from α2 to the beginning of α3 in native moPrP has become more stable. It became important to examine the kinetics of structural change in different segments of the protein structure and to determine where conformational conversion begins. In order to do so, HDX labeling pulses of 180-s (Fig. 7) as well as of 30-s (Fig. S6) duration were applied at different times of oligomerization.

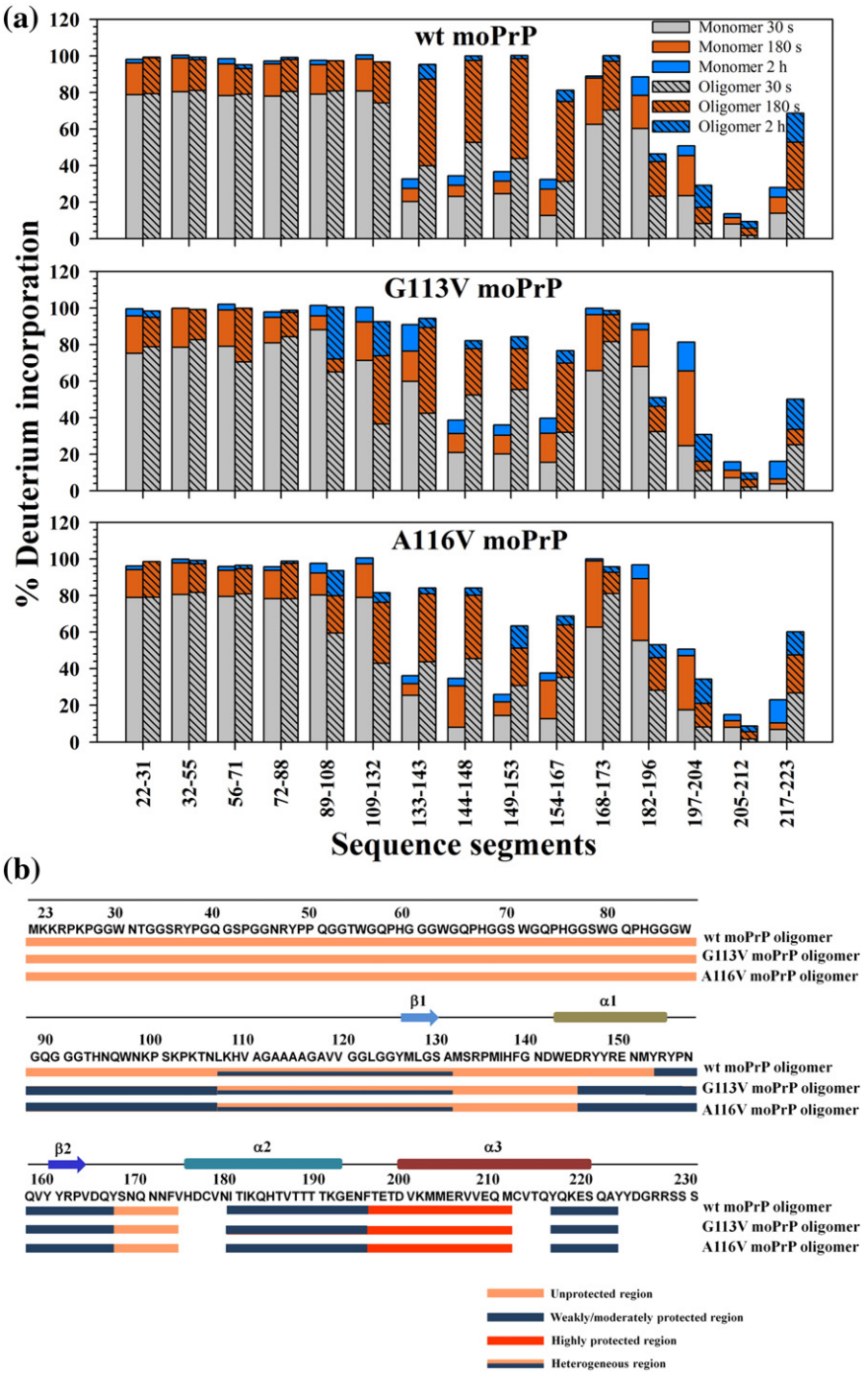

Fig. 6. HDX–MS characterization of the monomeric and oligomeric forms of the moPrP variants at pH 4. Oligomers were formed from 100 μM protein in the presence of 150 mM NaCl at 37 °C (pH 4). (a) Deuterium incorporation into different sequence segments of monomer (empty bars) and oligomer (stipled bars) of the moPrP variants is shown. The colors of the bar encode the extent of HDX labeling after different times of pulse labeling, which is showed in the first panel. (b) Mapping of the protection against HDX for the oligomers formed by the three moPrP variants to the sequence of moPrP. Sequence segments, highly protected (≤ 20% of deuterium incorporation after 180 s of HDX), weakly to moderately protected (20–80% of deuterium incorporation after 180 s of HDX), and unprotected (≥80% of deuterium incorporation after 180 s of HDX), are shown for wt, G113V, and A116V moPrP. The sequence segment exhibiting conformational heterogeneity in the three oligomers formed by the moPrP variants is also shown.

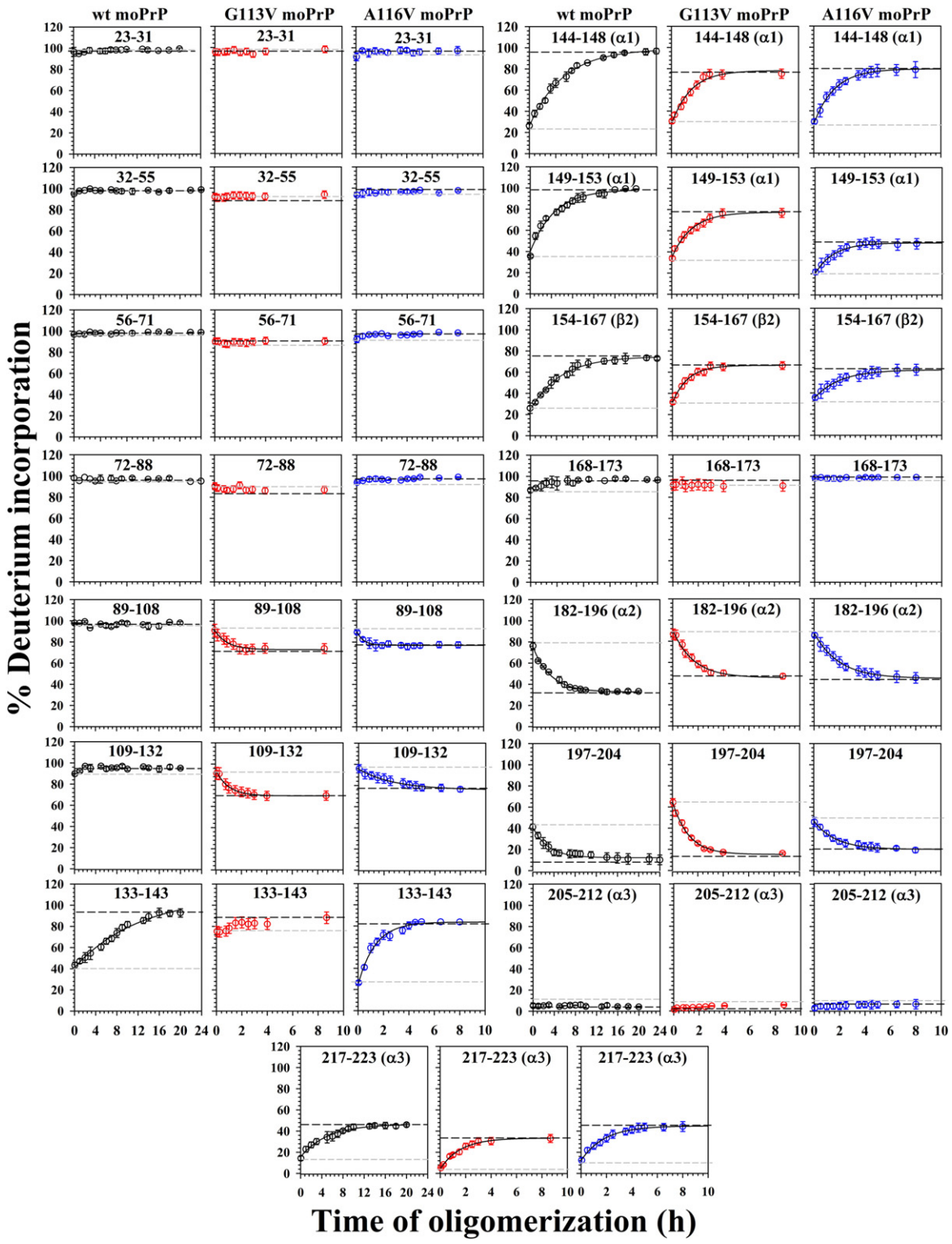

Fig. 7. Kinetics of pulsed HDX into different sequence segments of the moPrP variants during misfolding and oligomerization. Kinetics of pulsed HDX into different sequence segments of the moPrP variants during misfolding and oligomerization. Misfolding and oligomerization of the moPrP variants were initiated by the addition of 150 mM NaCl to 100 μM protein at 37 °C (pH 4). Percentage of deuterium incorporation *versus* time profiles, obtained using 180-s HDX labeling pulses, are shown for different sequence segments. The gray dashed line and the black dashed line represent the lower and upper boundary of the percentage of deuterium incorporation into each sequence segment, respectively (see Supporting Materials and Methods). Error bars represent the standard deviations determined from three independent experiments.

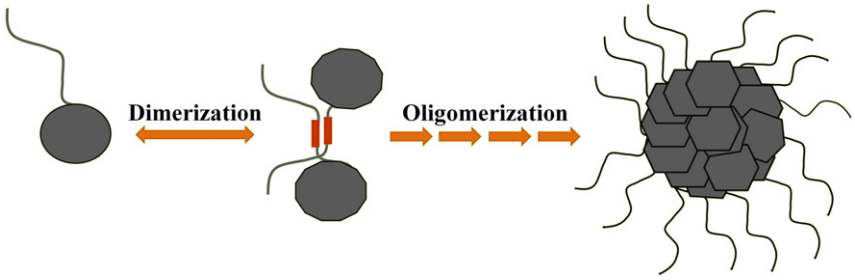

Fig. 8. Model for the formation of oligomers by the moPrP. Monomers interact in a rate-limiting step to form a dimer. The palindromic sequence becomes structured during the course of dimer and larger oligomer formation (see Results and Discussion). It is not known whether the dimer and oligomers grow by the addition of monomers, dimers, or both. Minor structural change in the CTD is shown to happen during dimer and oligomer formation, but major conformational conversion in the CTD occurs primarily in the oligomeric state. The nature of the structure that forms in the middle hydrophobic region during dimer formation is not known.

Conformational conversion in the CTD occurs slower than dimer and oligomer formation

In the case of all three moPrP variants, the rates of the change in protection of the individual sequence segments spanned the rates measured by CD (Table S2 and S3). For the mutant variants, the rates for gain in protection of sequence segments 89–108 and/or 109–132, which constitute the middle hydrophobic region, appeared to be faster than the rates for the change in protection of the other sequence segments. It is likely that it is the intermolecular association of the middle hydrophobic region that leads to the initial formation of a dimer, which constitutes the rate-limiting step in misfolding and oligomerization (see above). At present, it is not known whether structural change triggered in the middle hydrophobic region upon the addition of 150 mM NaCl occurs in the monomer prior to dimer formation or whether it accompanies dimer formation and oligomer growth. It should be noted that although sequence segment 205–212 became more strongly protected in the oligomers than in the monomer, the decrease in the extent of HDX was too small for the rate of its conformational change to be determined.

α1 appears to act as a gatekeeper subdomain controlling the conformational conversion in the CTD

An important result is that sequence segments 133–167 and 217–223 lost protection (see above) at the same rate at which sequence segment 182–204 gained protection. Sequence segment 133–167 spans α1 and the loop immediately following it in native moPrP, and earlier studies [7,45] had shown that several destabilizing pathogenic mutations accelerate misfolding by destabilizing and causing α1 to either unravel or move away from the α2–α3 subdomain before structural changes could occur elsewhere in the protein. This two-stage mechanism [7] is also supported by studies on wt moPrP and other mutant variants [26,46]. In the current kinetic study, all parts of the CTD appeared to undergo conformational change at the same rate, but this observation can be reconciled with the two-stage mechanism by positing that the unraveling of α1 (Stage 1) is the rate-limiting step and that conformational changes in other secondary structural segments (Stage II) follow rapidly thereafter. It seems that α1 acts as a gatekeeper subdomain, preventing the hydrophobic surface on α2–α3 subdomain from becoming hydrated [47,48,49] and preventing its destabilization [38,50] and subsequent misfolding. When α1 is caused to either unravel or be pushed away from the α2–α3 subdomain by pathogenic mutations, misfolding is accelerated.

In summary, the present study shows that the pathogenic mutations, G113V and A116V, in the palindromic region of moPrP may induce prion pathogenesis by accelerating misfolding and aggregation. Both mutations are able to do this by inducing structure in the palindromic region, which appears to be a site for intermolecular association in the oligomers. This study suggests that conformational conversion occurs in oligomeric protein (Fig. 8). Reconciling the kinetic data of this study with previous mutational data suggests that α1 acts as a gatekeeper controlling the conformational conversion.

Materials and Methods

Buffers and reagents

All the reagents and buffers were of the highest purity grade and were obtained from Sigma Aldrich, unless otherwise specified. The guanidine hydrochloride (Molecular Biology grade) used for the purification of the full-length moPrP variants was obtained from HiMedia.

Site-directed mutagenesis

The mutant variants of full-length moPrP were generated using the QuikChange® site-directed mutagenesis kit (Stratagene). Primers containing 1–2 nucleotide changes were obtained from Sigma. The mutations in the plasmids were confirmed by DNA sequencing.

Protein expression and purification

Wt moPrP and the two mutant variants were expressed in *Escherichia coli* BL21 (DE3) codon plus (Stratagene) cells transformed with a pET17b plasmid containing the full-length sequence (23–231) of the moPrP gene. The moPrP variants were purified as described previously [29]. The purity of each moPrP variant preparation was confirmed by MS. Each moPrP variant had the expected mass indicating that no chemical modification had taken place in any of the variants.

Far-UV CD measurements

A Jasco J-815 CD spectropolarimeter was used for the far-UV CD measurements, using a quartz cuvette of 1-mm path length. The protein concentration was 10 μM in 10 mM NaOAc buffer (pH 4). The instrument settings were: digital integration time, 1 s; bandwidth, 1 nm; wavelength scan, 200–250 nm; and scanning rate, 50 nm/min.

FTIR spectroscopy

FTIR measurements were carried out using a Thermo Nicolet-6700 FTIR spectrometer (Thermo Scientific) equipped with a liquid-nitrogen-cooled Mercury Cadmium Telluride (MCT) detector. The spectrometer was purged with ultrapure nitrogen gas. Solutions of wt, G113V, and A116V moPrP, both native monomeric and oligomeric forms, were used for the measurements. Concentrated protein samples (≈1 mM) were applied directly onto a diamond crystal and were dried using ultrapure nitrogen gas. Spectra were recorded in the attenuated total reflectance mode at a resolution of 4 cm^{-1}. Before each sample acquisition, a buffer spectrum was recorded under identical conditions and was used as the blank. For each sample, 2048 scans were averaged.

Denaturant-induced equilibrium unfolding studies

Urea- and GdnHCl-induced equilibrium unfolding transitions were carried out at pH 4 (in 10 mM sodium acetate buffer) and at pH 7 (in 50 mM Tris–HCl buffer). For these studies, 10 μM protein was incubated in different concentrations of denaturant for 2 h at 25 °C before the change in the far-UV CD signal was monitored at 222 nm and at other wavelengths using the Jasco J-815 spectropolarimeter. The data were fit to a two-state (N ↔ U) equilibrium unfolding model [51], and the thermodynamic parameters were obtained. It should be noted that for all three moPrP variants, the measured unfolding transition corresponds to that of the structured CTD of the protein.

Thermal equilibrium unfolding studies

Thermally induced equilibrium unfolding transitions were monitored at pH 4 in 10 mM sodium acetate buffer by measuring the change in the CD signal at 222 nm using the Jasco J-815 spectropolarimeter. In a 1-mm cuvette, 10 μM protein was used, and the temperature scanning rate was 1 °C /min.

Oligomerization and misfolding studies at pH 4

The oligomerization and misfolding studies were carried out as described earlier [25]. Briefly, the protein in 10 mM sodium acetate buffer (pH 4) was diluted twofold with 2 × aggregation buffer [10 mM sodium acetate buffer and 300 mM NaCl (pH 4)], so that the protein was finally in 1 × aggregation buffer [10 mM sodium acetate buffer and 150 mM NaCl (pH 4)]. The samples were then incubated at 37 °C. The final protein concentration used for the experiments was 10–100 μM. Oligomerization at different time points was monitored by SEC. For studying the extent of oligomerization, a 100-μL aliquot of the incubated sample was injected into a Waters Protein Pak 300-SW column using an Akta (GE) chromatography system kept at 25 °C. The column was equilibrated with four column volumes of 1 × aggregation buffer at pH 4 (10 mM sodium acetate buffer and 150 mM NaCl), after several samples of oligomer had first been run through the column. In all subsequent SEC experiments, the amounts of oligomer and monomer that eluted were found to account for all the protein that had been injected into the column. The areas under the monomer and oligomer peaks were calculated by fitting the SEC profiles (monitored by absorbance at 280 nm) to multiple Gaussian peaks using Origin Pro 8. The fraction monomer left was calculated from the area under the monomer peak and then divided by the total area under all the peaks. The fraction oligomer formed was then calculated by subtracting the fraction monomer from 1. Concurrently, the samples were diluted to 10 μM in 1 × aggregation buffer, and the far-UV CD spectra were acquired using the parameters mentioned above. The misfolding and oligomerization rates were obtained by fitting the fraction misfolded, which was obtained from the change in CD signal at 222 nm, or the fraction of oligomer, which was obtained from the SEC profiles, to a single exponential equation to obtain the rates of misfolding and oligomerization, respectively.

Determination of the initial rates and reaction order for misfolding and oligomerization

For initial rate determination, the first 10% of the normalized data for each protein concentration (ranging from 10 to 100 μM) was fit to a straight line equation. The slope obtained was the initial rate per unit concentration. The slope of a linear fit of log initial rate *versus* log initial monomer concentration is equal to n – 1 [See Eq. (1)] [52].

$$\log\left(\frac{v_0}{C_0}\right) = \log k + (n-1)\log C_0 \quad (1)$$

v_0 is the initial rate obtained from the linear fits, C_0 is the initial protein concentration, k is the rate constant, and n is the true reaction order with respect to monomer concentration.

DLS measurements

DLS measurements were carried out on a DynaPro-99 unit (Wyatt Technology Corp.) All the buffers were filtered through 0.02-μm filters from Whatman. The scattering intensity at right angles and its autocorrelation were acquired simultaneously using a laser at 829.4 nm to illuminate the sample. For the experiments, 60 acquisitions were collected at each time point. The acquisition time was set at 5 s, the signal-to-noise threshold at 2.5, the temperature at 25 °C, and the sensitivity at 100%. Data with uneven autocorrelation functions were excluded. The data were then resolved into a Gaussian distribution using DynaLS (Protein Solutions Ltd.).

Native state HDX–MS measurements

The peptide map of moPrP variants was generated as described earlier [34]. To initiate deuterium labeling, a 100-μM protein sample was diluted 20-fold into a labeling buffer [10 mM sodium acetate buffer in D_2O (pH 4) corrected for isotope effect) so that the protein was in 95% D_2O and was incubated at 25 °C. At different times of labeling, a 50-μL aliquot was withdrawn from the labeling reaction and was mixed with 50 μL of ice-cold 20 mM glycine–HCl buffer (pH 2.5) to quench the labeling. These samples were then immediately injected into the HDX module (Waters) coupled with a nano Acquity UPLC for online pepsin digestion using an immobilized pepsin cartridge (Applied Biosystems). Further processing of the sample for mass determination using a Waters Synapt G2 mass spectrometer was carried out as described earlier [34]. The extent of deuterium incorporation into different segments at each time point was calculated as described below.

Oligomerization kinetics monitored using HDX–MS measurements

To initiate deuterium labeling, a 20-μL aliquot was withdrawn from the aggregation reaction, diluted into 180 μL of aggregation buffer prepared in D_2O [150 mM NaCl in 10 mM NaOAc buffer (pH 4) corrected for the isotope effect], and incubated at 37 °C. After labeling for 30 s, 180 s, or 2 h, 200-μL samples were mixed with 400 μL of ice-cold 8.0 M GdnHCl in 100 mM glycine buffer (pH 2.5) to dissolve the aggregate. After 2 min of incubation on ice, the samples were desalted using a Sephadex G-25 HiTrap desalting column equilibrated with water (pH 2.5), with an Akta Basic HPLC. The desalted samples were injected into the HDX module (Waters) coupled with a nanoAcquity UPLC for online pepsin digestion using an immobilized pepsin cartridge (Applied Biosystems). Further processing of the sample for mass determination using a Waters Synapt G2 mass spectrometer was carried out as described earlier [44].

Peptide masses were calculated from the centroid of the isotopic envelope using the MassLynx software, and the shift in the mass of labeled peptide relative to the unlabeled peptide was used to determine the extent of deuterium incorporation at each time of application of the HDX labeling pulse. As the sample was in 90% D_2O during labeling and was exposed to H_2O after dissolution in GdnHCl, control experiments were carried out to correct for back exchange and forward exchange. To this end, moPrP was incubated in 10 mM sodium acetate at pH 4 (90% D_2O) and was fully deuterated by unfolding at 65 °C for 10 min, followed by refolding on ice. Refolded moPrP was shown to be identical to native moPrP. The fully deuterated moPrP sample was then processed in exactly the same way as the aggregates. The extent of deuterium incorporation in each peptide, % *D*, was determined using the equation $\% D = (m(t) - m(0\%))/(m(90\%) - m(0\%)) \times 100$, where $m(t)$ is the measured centroid mass of the peptide at time point t, $m(0\%)$ is the measured mass of an undeuterated reference sample, and $m(90\%)$ is the measured mass of a fully deuterated reference sample (in 90% D_2O). The plot of the percentage of deuterium incorporation *versus* time of oligomerization for each protein sequence segments was used for deducing the rate of deuterium incorporation by fitting with a single exponential function. The lower and upper boundary of deuterium incorporation was marked by using the percentage of deuterium incorporation into the monomer (in the absence of 150 mM NaCl) and preformed oligomer, respectively.

The percentage of deuterium incorporation for peptides showing a bimodal distribution was calculated as described earlier [34]. Briefly, for calculation of the percentage protected and the accessible forms of a peptide, the bimodal isotopic peaks were fitted to the individual isotopic peak as a sum of two Gaussian distributions using OriginPro 8. The percentage of each form was calculated from the relative area under each peak.

Acknowledgments

We thank the members of our laboratory for discussion and for their comments on the manuscript. J.B.U. is a recipient of a JC Bose National Fellowship from the Government of India. This work was funded by the Tata Institute of Fundamental Research and by the Department of Biotechnology, Government of India.

Appendix A. Supplementary Data

Supplementary data to this article can be found online at http://dx.doi.org/10.1016/j.jmb.2016.08.015.

Received 23 June 2016;
Received in revised form 9 August 2016;
Accepted 12 August 2016
Available online 18 August 2016

Keywords:
cellular prion protein;
circular dichroism;
hydrogen–deuterium exchange–mass spectrometry;
size-exclusion chromatography;

Abbreviations used:
PrP^C, cellular prion protein; PrP^{Sc}, aggregated form of prion protein; NTR, N-terminal region; CTD, C-terminal domain; α2, helix 2; α3, helix 3; CD, circular dichroism; FTIR, Fourier transform infrared; DLS, dynamic light scattering; wt, wild-type; SEC, size-exclusion chromatography; HDX, hydrogen–deuterium exchange; MS, mass spectrometry.

References

[1] A. Aguzzi, M. Polymenidou, Mammalian prion biology: one century of evolving concepts, Cell 116 (2004) 313–327.
[2] F.E. Cohen, S.B. Prusiner, Pathologic conformations of prion proteins, Annu. Rev. Biochem. 67 (1998) 793–819.
[3] S.B. Prusiner, Molecular biology of prion diseases, Science 252 (1991) 1515–1522.
[4] R. Zahn, A. Liu, T. Luhrs, R. Riek, C. von Schroetter, F. Lopez Garcia, M. Billeter, L. Calzolai, G. Wider, K. Wuthrich, NMR solution structure of the human prion protein, Proc. Natl. Acad. Sci. U. S. A. 97 (2000) 145–150.
[5] S.B. Prusiner, D.F. Groth, D.C. Bolton, S.B. Kent, L.E. Hood, Purification and structural studies of a major scrapie prion protein, Cell 38 (1984) 127–134.
[6] S. Mead, Prion disease genetics, Eur. J. Hum. Genet. 14 (2006) 273–281.
[7] J. Singh, J.B. Udgaonkar, Structural effects of multiple pathogenic mutations suggest a model for the initiation of misfolding of the prion protein, Angew. Chem. 127 (2015) 7639–7643.
[8] S. Liemann, R. Glockshuber, Influence of amino acid substitutions related to inherited human prion diseases on the thermodynamic stability of the cellular prion protein, Biochemistry 38 (1999) 3258–3267.
[9] A.C. Apetri, K. Surewicz, W.K. Surewicz, The effect of disease-associated mutations on the folding pathway of human prion protein, J. Biol. Chem. 279 (2004) 18,008–18,014.
[10] D. Peretz, R.A. Williamson, Y. Matsunaga, H. Serban, C. Pinilla, R.B. Bastidas, R. Rozenshteyn, T.L. James, R.A. Houghten, F.E. Cohen, A conformational transition at the N terminus of the prion protein features in formation of the scrapie isoform, J. Mol. Biol. 273 (1997) 614–622.
[11] C. Hölscher, H. Delius, A. Bürkle, Overexpression of nonconvertible PrP c Δ114–121 in scrapie-infected mouse neuroblastoma cells leads to trans-dominant inhibition of wild-type PrP Sc accumulation, J. Virol. 72 (1998) 1153–1159.
[12] M.F. Jobling, L.R. Stewart, A.R. White, C. McLean, A. Friedhuber, F. Maher, K. Beyreuther, C.L. Masters, C.J. Barrow, S.J. Collins, The hydrophobic core sequence modulates the neurotoxic and secondary structure properties of the prion peptide 106–126, J. Neurochem. 73 (1999) 1557–1565.
[13] K. Kuwata, T. Matumoto, H. Cheng, K. Nagayama, T.L. James, H. Roder, NMR-detected hydrogen exchange and molecular dynamics simulations provide structural insight into fibril formation of prion protein fragment 106–126, Proc. Natl. Acad. Sci. 100 (2003) 14,790–14,795.
[14] K.H. Lim, T.N. Nguyen, S.M. Damo, T. Mazur, H.L. Ball, S.B. Prusiner, A. Pines, D.E. Wemmer, Solid-state NMR structural studies of the fibril form of a mutant mouse prion peptide PrP 89–143 (P101L), Solid State Nucl. Magn. Reson. 29 (2006) 183–190.
[15] E.M. Norstrom, J.A. Mastrianni, The AGAAAAGA palindrome in PrP is required to generate a productive PrPSc–PrPC complex that leads to prion propagation, J. Biol. Chem. 280 (2005) 27,236–27,243.
[16] I.H. Solomon, J.A. Schepker, D.A. Harris, Prion neurotoxicity: insights from prion protein mutants, Curr. Issues Mol. Biol. 12 (2010) 51–61.
[17] R.S. Hegde, J.A. Mastrianni, M.R. Scott, K.A. DeFea, P. Tremblay, M. Torchia, S.J. DeArmond, S.B. Prusiner, V.R. Lingappa, A transmembrane form of the prion protein in neurodegenerative disease, Science, 279 (1998) 827–834.
[18] R.S. Hegde, P. Tremblay, D. Groth, S.J. DeArmond, S.B. Prusiner, V.R. Lingappa, Transmissible and genetic prion diseases share a common pathway of neurodegeneration, Nature 402 (1999) 822–826.
[19] A.T. Sabareesan, J. Singh, S. Roy, J.B. Udgaonkar, M. Mathew, The pathogenic A116V mutation enhances ion-selective channel formation by prion protein in membranes, Biophys. J. 110 (2016) 1766–1776.
[20] B.R. Groveman, A. Kraus, L.D. Raymond, M.A. Dolan, K.J. Anson, D.W. Dorward, B. Caughey, Charge neutralization of the central lysine cluster in prion protein (PrP) promotes PrPSc-like folding of recombinant PrP amyloids, J. Biol. Chem. 290 (2015) 1119–1128.
[21] B.M. Coleman, C.F. Harrison, B. Guo, C.L. Masters, K.J. Barnham, V.A. Lawson, A.F. Hill, Pathogenic mutations within the hydrophobic domain of the prion protein lead to the formation of protease-sensitive prion species with increased lethality, J. Virol. 88 (2014) 2690–2703.
[22] R. Moulick, J.B. Udgaonkar, Thermodynamic characterization of the unfolding of the prion protein, Biophys. J. 106 (2014) 410–420.
[23] W. Swietnicki, R.B. Petersen, P. Gambetti, W.K. Surewicz, Familial mutations and the thermodynamic stability of the recombinant human prion protein, J. Biol. Chem. 273 (1998) 31,048–31,052.
[24] J.E. Arnold, C. Tipler, L. Laszlo, J. Hope, M. Landon, R.J. Mayer, The abnormal isoform of the prion protein accumulates in late-endosome-like organelles in scrapie-infected mouse brain, J. Pathol. 176 (1995) 403–411.
[25] J. Singh, H. Kumar, A.T. Sabareesan, J.B. Udgaonkar, Rational stabilization of helix 2 of the prion protein prevents its misfolding and oligomerization, J. Am. Chem. Soc. 136 (2014) 16,704–16,707.
[26] J. Singh, J.B. Udgaonkar, Unraveling the molecular mechanism of pH-induced misfolding and oligomerization of the prion protein, J. Mol. Biol. 428 (2016) 1345–1355.
[27] L.L. Hosszu, M.H. Tattum, S. Jones, C.R. Trevitt, M.A. Wells, J.P. Waltho, J. Collinge, G.S. Jackson, A.R. Clarke, The H187R mutation of the human prion protein induces conversion of recombinant prion protein to the PrPSc-like form, Biochemistry, 49 (2010) 8729–8738.
[28] M.Q. Khan, B. Sweeting, V.K. Mulligan, P.E. Arslan, N.R. Cashman, E.F. Pai, A. Chakrabartty, Prion disease susceptibility is affected by β-structure folding propensity and local side-chain interactions in PrP, Proc. Natl. Acad. Sci. 107 (2010) 19,808–19,813.
[29] S. Jain, J.B. Udgaonkar, Evidence for stepwise formation of amyloid fibrils by the mouse prion protein, J. Mol. Biol. 382 (2008) 1228–1241.
[30] A.K. Thakur, M. Jayaraman, R. Mishra, M. Thakur, V.M. Chellgren, I.J. Byeon, D.H. Anjum, R. Kodali, T.P. Creamer, J.F. Conway, A.M. Gronenborn, R. Wetzel, Polyglutamine disruption of the huntingtin exon 1 N terminus triggers a

complex aggregation mechanism, Nat. Struct. Mol. Biol. 16 (2009) 380–389.
[31] L. Konermann, J. Pan, Y.-H. Liu, Hydrogen exchange mass spectrometry for studying protein structure and dynamics, Chem. Soc. Rev. 40 (2011) 1224–1234.
[32] Y. Bai, J.S. Milne, L. Mayne, S.W. Englander, Primary structure effects on peptide group hydrogen exchange, Proteins Struct. Funct. Bioinf. 17 (1993) 75–86.
[33] S.-H. Bae, G. Legname, A. Serban, S.B. Prusiner, P.E. Wright, H.J. Dyson, Prion proteins with pathogenic and protective mutations show similar structure and dynamics, Biochemistry 48 (2009) 8120–8128.
[34] J. Singh, A.T. Sabareesan, M.K. Mathew, J.B. Udgaonkar, Development of the structural core and of conformational heterogeneity during the conversion of oligomers of the mouse prion protein to worm-like amyloid fibrils, J. Mol. Biol. 423 (2012) 217–231.
[35] R.N. Abskharon, G. Giachin, A. Wohlkonig, S.H. Soror, E. Pardon, G. Legname, J. Steyaert, Probing the N-terminal β-sheet conversion in the crystal structure of the human prion protein bound to a nanobody, J. Am. Chem. Soc. 136 (2014) 937–944.
[36] J. Ziegler, C. Viehrig, S. Geimer, P. Rösch, S. Schwarzinger, Putative aggregation initiation sites in prion protein, FEBS Lett. 580 (2006) 2033–2040.
[37] M. Gasset, M.A. Baldwin, D.H. Lloyd, J.-M. Gabriel, D.M. Holtzman, F. Cohen, R. Fletterick, S.B. Prusiner, Predicted alpha-helical regions of the prion protein when synthesized as peptides form amyloid, Proc. Natl. Acad. Sci. 89 (1992) 10,940–10,944.
[38] I. Hafner-Bratkovič, R. Bester, P. Pristovšek, L. Gaedtke, P. Veranič, J. Gašperšič, M. Manček-Keber, M. Avbelj, M. Polymenidou, C. Julius, Globular domain of the prion protein needs to be unlocked by domain swapping to support prion protein conversion, J. Biol. Chem. 286 (2011) 12,149–12,156.
[39] V. Smirnovas, G.S. Baron, D.K. Offerdahl, G.J. Raymond, B. Caughey, W.K. Surewicz, Structural organization of brain-derived mammalian prions examined by hydrogen–deuterium exchange, Nat. Struct. Mol. Biol. 18 (2011) 504–506.
[40] S. Simoneau, H. Rezaei, N. Salès, G. Kaiser-Schulz, M. Lefebvre-Roque, C. Vidal, J.-G. Fournier, J. Comte, F. Wopfner, J. Grosclaude, *In vitro* and *in vivo* neurotoxicity of prion protein oligomers, PLoS Pathog. 3 (2007), e125.
[41] F. Sokolowski, A.J. Modler, R. Masuch, D. Zirwer, M. Baier, G. Lutsch, D.A. Moss, K. Gast, D. Naumann, Formation of critical oligomers is a key event during conformational transition of recombinant Syrian hamster prion protein, J. Biol. Chem. 278 (2003) 40,481–40,492.
[42] K.-M. Pan, M. Baldwin, J. Nguyen, M. Gasset, A. Serban, D. Groth, I. Mehlhorn, Z. Huang, R.J. Fletterick, F.E. Cohen, Conversion of alpha-helices into beta-sheets features in the formation of the scrapie prion proteins, Proc. Natl. Acad. Sci. 90 (1993) 10,962–10,966.
[43] H. Wille, M.D. Michelitsch, V. Guenebaut, S. Supattapone, A. Serban, F.E. Cohen, D.A. Agard, S.B. Prusiner, Structural studies of the scrapie prion protein by electron crystallography, Proc. Natl. Acad. Sci. U. S. A. 99 (2002) 3563–3568.
[44] J. Singh, J.B. Udgaonkar, Dissection of conformational conversion events during prion amyloid fibril formation using hydrogen exchange and mass spectrometry, J. Mol. Biol. 425 (2013) 3510–3521.
[45] J. Singh, J.B. Udgaonkar, The pathogenic mutation T182 A converts the prion protein into a molten globule-like conformation whose misfolding to oligomers but not to fibrils is drastically accelerated, Biochemistry 55 (2016) 459.
[46] R. Moulick, R. Das, J.B. Udgaonkar, Partially unfolded forms of the prion protein populated under misfolding-promoting conditions: characterization by hydrogen exchange mass spectrometry and NMR, J. Biol. Chem. 290 (2015) 25,227–25,240.
[47] A. De Simone, A. Zagari, P. Derreumaux, Structural and hydration properties of the partially unfolded states of the prion protein, Biophys. J. 93 (2007) 1284–1292.
[48] A. De Simone, G.G. Dodson, C.S. Verma, A. Zagari, F. Fraternali, Prion and water: tight and dynamical hydration sites have a key role in structural stability, Proc. Natl. Acad. Sci. U. S. A. 102 (2005) 7535–7540.
[49] M.P. Morrissey, E.I. Shakhnovich, Evidence for the role of PrP(C) helix 1 in the hydrophilic seeding of prion aggregates, Proc. Natl. Acad. Sci. U. S. A. 96 (1999) 11,293–11,298.
[50] N. Chakroun, S. Prigent, C.A. Dreiss, S. Noinville, C. Chapuis, F. Fraternali, H. Rezaei, The oligomerization properties of prion protein are restricted to the H2H3 domain, FASEB J. 24 (2010) 3222–3231.
[51] V.R. Agashe, J.B. Udgaonkar, Thermodynamics of denaturation of barstar: evidence for cold denaturation and evaluation of the interaction with guanidine hydrochloride, Biochemistry 34 (1995) 3286–3299.
[52] R.M. Murphy, A.M. Tsai, Misbehaving Proteins: Protein (Mis)Folding, Aggregation, and Stability, Springer, New York, 2006 (ISBN 978-0-387-36063-8).
[53] C.A. Roach, J.V. Simpson, R.D. JiJi, Evolution of quantitative methods in protein secondary structure determination *via* deep-ultraviolet resonance Raman spectroscopy, Analyst 137 (2012) 555–562.